Reaction Chemistry in the Afterglow of an Oxygen−Helium, Atmospheric-Pressure Plasma

James Y. Jeong,[†] Jaeyoung Park,[‡] Ivars Henins,[‡] Steve E. Babayan,[†] Vincent J. Tu,[†] Gary S. Selwyn,[‡] Guowen Ding,[†] and Robert F. Hicks*,[†]

Chemical Engineering Department, University of California, Los Angeles, California 90095, and Plasma Physics, Los Alamos National Laboratory, Los Alamos, New Mexico 87545

Received: March 31, 2000

The reaction chemistry in the afterglow of a non-equilibrium, capacitive discharge, operated at 600 Torr total pressure with $(0.5 \text{ to } 5.0) \times 10^{17}$ cm^{-3} of oxygen in helium, has been examined by ultraviolet absorption spectroscopy, optical emission spectroscopy, and numerical modeling. The densities of the active species, $O(^3P)$, $O_2(^1\Delta_g)$, $O_2(^1\Sigma_g^+)$, and O_3, have been determined as a function of the operating conditions. At RF power densities between 6.1 and 30.5 W/cm^3 and a neutral temperature of 100 ± 40 °C, the plasma generated $(0.2 \text{ to } 1.0) \times 10^{16}$ cm^{-3} of $O(^3P)$ and $O_2(^1\Delta_g)$, $(0.2 \text{ to } 2.0) \times 10^{15}$ cm^{-3} of $O_2(^1\Sigma_g^+)$, and $(0.1 \text{ to } 4.0) \times 10^{15}$ cm^{-3} of O_3. After the power was turned off, the singlet-sigma and singlet-delta states decayed within 0.1 and 30.0 ms, respectively. The concentration of oxygen atoms remained constant for about 0.5 ms, then fell rapidly due to recombination with O_2 to form O_3. It was found that the etching rate of polyimide correlated with the concentration of oxygen atoms in the afterglow, indicating that the O atoms were the active species involved in this process.

I. Introduction

Oxygen plasmas, containing 1−10 Torr of O_2, are widely used for ashing photoresist films on semiconductor wafers.[1−3] In this process, the substrate is placed downstream of the region of gas excitation, since it is undesirable for ions to bombard the substrate and potentially damage the thin dielectric layers. Although the afterglow region of oxygen plasmas has been studied for a long time,[4−7] there are still many uncertainties with regard to the reaction chemistry, particularly how the distribution of reactive oxygen species affects materials processes carried out downstream. Today, complex photoresists are being developed to transfer smaller and smaller patterns onto semiconductor surfaces.[8] This requires that the plasma chemistry be fine-tuned to selectively etch the material without attacking and undercutting any of the underlying films. A thorough knowledge of the reaction chemistry would greatly assist in the achievement of this goal.

Recently, we have developed a plasma source that operates at atmospheric pressure and neutral temperatures between 100 and 200 °C.[9−12] A stable, homogeneous, arc-less gas discharge was created by flowing gas composed primarily of helium between two closely spaced metal electrodes driven with RF power at 13.56 MHz. Addition of 1 to 10 Torr of oxygen to the gas feed yielded a high concentration of reactive species that was capable of etching polyimide and other organic films at rates in excess of 10 μm/min.[9,10] In this regard, our source was similar to a pure oxygen discharge operated at 1 to 10 Torr total pressure. However, an atmospheric-pressure plasma can offer several advantages over a low-pressure plasma, such as reduced ion damage.

In this paper, we have characterized the afterglow of an atmospheric-pressure oxygen plasma using time-resolved ultraviolet absorption and optical emission spectroscopy, and nu-

merical modeling of the reaction kinetics. This approach provides a new method for determining the concentration of ground-state oxygen atoms in a downstream plasma process. Ten microseconds after turning off the RF power, the reaction mechanism may be adequately described with six species: ground-state O_2, ground-state He, ground-state O atoms (^3P), metastable molecular O_2 ($^1\Delta_g$ and $^1\Sigma_g^+$), and ozone. The dependence of the latter four reactive species on the plasma operating conditions has been determined. These results are important for understanding how atmospheric-pressure plasmas may be utilized in semiconductor processing, e.g., for the ashing of photoresist films.

II. Experimental Methods

Apparatus. A schematic of the plasma source used in this study is presented in Figure 1. It consisted of two parallel-plate electrodes made of aluminum, and separated by a gap 1.6 mm in height. The lower electrode was 10.2 cm wide by 5.5 cm long and was driven by RF power at 13.56 MHz, while the upper electrode was 10.2 cm wide by 20.4 cm long and was grounded. Just downstream of the lower electrode was an aluminum oxide plate, 10.2×10.2 cm^2, which avoided any disturbance of the gas flow in the afterglow region. The sides of the duct parallel to the flow direction were sealed with quartz windows so that spectroscopic measurements of the gas could be made. A slit was placed across the flow path upstream of the plasma to provide for a uniform flow velocity across the duct. The neutral gas temperature was recorded as a function of the process conditions with an ungrounded thermocouple, 0.8 mm in diameter. To make the measurement, it was momentarily inserted into the gas flow just 5 mm downstream of the powered electrode.

The plasma was operated with helium and oxygen gas mixtures at 600 Torr total pressure (ambient conditions at Los Alamos National Laboratory), and a flow velocity of 5.2 m/s (at 25 °C and 600 Torr). This corresponds to a Reynold's

* To whom correspondence should be addressed. E-mail: rhicks@ucla.edu.
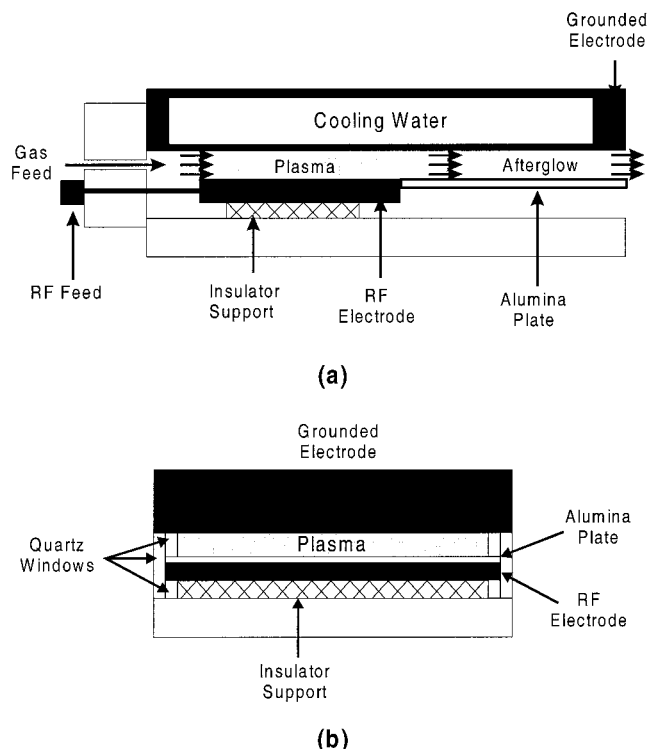† University of California.
‡ Los Alamos National Laboratory.

Figure 1. Schematic of the parallel-plate plasma: (a) side view, and (b) front view.
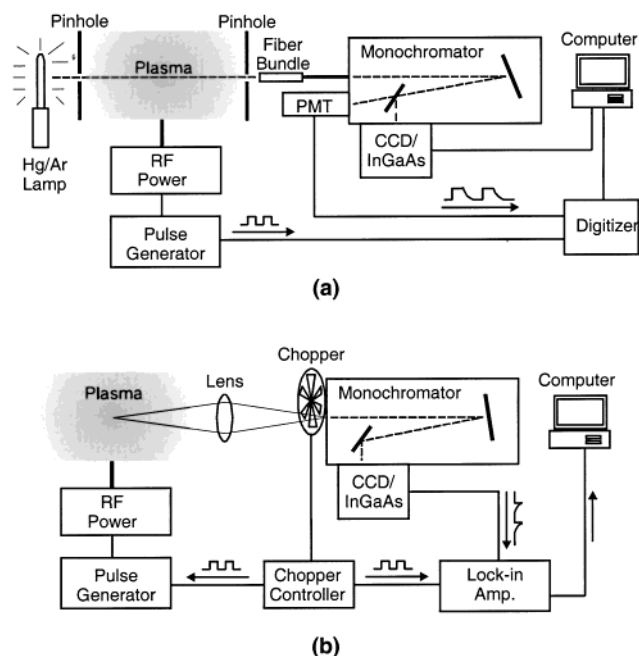

Figure 2. Diagram of the apparatus used for (a) time-resolved UV absorption and optical emission spectroscopy, and (b) time-averaged infrared emission spectroscopy without interference from background emission from the plasma.

number of 22.4, which is well within the laminar-flow regime. The oxygen partial pressure in the plasma was varied from 1.0 to 15.0 Torr, while holding the RF power constant at 400 W (24.4 W/cm³) and the gas temperature at 120 °C. Conversely, the RF power was varied from 100 to 500 W (6.1 to 30.5 W/cm³), while keeping the oxygen partial pressure at 6.0 Torr. The gas temperature depended on the applied power, increasing from 50 °C at 100 W to 140 °C at 500 W.

Ozone. Ultraviolet absorption spectroscopy was used to acquire the ozone concentration in the plasma and the downstream afterglow as a function of the process conditions. A schematic of the optical setup is shown in Figure 2 a. A mercury/argon lamp was mounted on one side of the plasma, while a quartz fiber-optic bundle was placed on the other side. Pinholes, approximately 1 mm in diameter, were placed in front of the lamp and the bundle to eliminate any stray light. Light passed through the fiber-optic bundle into a monochromator, and then was detected by either a UV-enhanced, charged-coupled device (CCD), or a photomultiplier tube (PMT). The monochromator had a focal length of 640 mm, a slit width of 150 μm, and a grating with 2400 grooves/mm. The average absolute concentration of the ozone in the plasma was calculated from the reduction in the Hg I emission intensity at 253.7 nm. It is noted that the absorption cross-section of O_3 at this wavelength, 1.16×10^{-17} cm², is much larger than the absorption cross-section of the weak Herzberg continuum of O_2, $< 1 \times 10^{-23}$ cm².[13-15]

The concentration of ozone was obtained either as a function of axial position during discharge operation, or as a function of time after extinguishing the plasma. For spatially resolved measurements, the intensity of the line at 253.7 nm was recorded with the CCD, and a spatial resolution of 3 mm was achieved. For temporally resolved measurements, the light intensity was recorded with the PMT to provide a fast response. The rise time of the photomultiplier tube was 2.3 ns, and the response time of the circuit was 1 μs. The signal was then digitized at 500 kHz to provide a time resolution of 2 μs, while the accuracy of

the triggering was better than 1 μs. Transient signals collected this way were average over 16 traces. The discharge was pulsed at 0.5 Hz with a 50% duty cycle for the afterglow experiments. This ensured that steady state was achieved prior to plasma extinction.

Singlet-Sigma Metastable Oxygen. Optical emission spectroscopy was used to record the concentration of singlet-sigma metastable oxygen, O_2 ($^1\Sigma_g^+$), and the R and P branches are centered at 759.9 and 764.5 nm. The same optical setup was used in this case as shown in Figure 2a, except that a slit, 0.1 mm $\times$ 0.086 mm, was substituted for the pinhole in front of the fiber-optic bundle. The emission intensity recorded by the monochromator and CCD detector in this region of the spectrum was calibrated with a NIST-traceable, standard tungsten lamp. The integrated intensity, $\bar{I}$, measured by the spectrometer from 757 to 773 nm is given by

$$\bar{I}_{lamp} = \int I_{lamp} \, d\lambda = kF_{lamp} \times \frac{1}{4\pi} \times \int S \, dA \qquad (1)$$

where I is the signal intensity recorded, λ is the wavelength (nm), k is the spectrometer calibration constant (nm s/photon), F is the photon flux of the lamp, 2.78×10^{17} photons mm² s⁻¹, S is the solid angle viewed through the slit, and A is the area (mm²) of the lamp sampled.

The integrated intensity of the light emitted by the metastable oxygen is

$$\bar{I}_{\Sigma} = \int I_{\Sigma} \, d\lambda = kR_{\Sigma} \times \frac{1}{4\pi} \times \int S \, dV \qquad (2)$$

where R_{Σ} is the rate of photon emission of the $^1\Sigma_g^+$ state (photons mm⁻¹ s⁻¹), and V is the volume (mm³) of the plasma sampled. The rate of photon emission for the transition $O_2(b^1\Sigma_g^+)$ to $O_2(X^3\Sigma_g^-)$ depends on the Einstein A-coefficient, A_Σ, and the excited species density, $[O_2 (b^1\Sigma_g^+)]$ as

$$R_{\Sigma} = A_{\Sigma} [O_2(b^1\Sigma_g^+)] \qquad (3)$$

Reactions in Afterglow of Oxygen−Helium Plasma

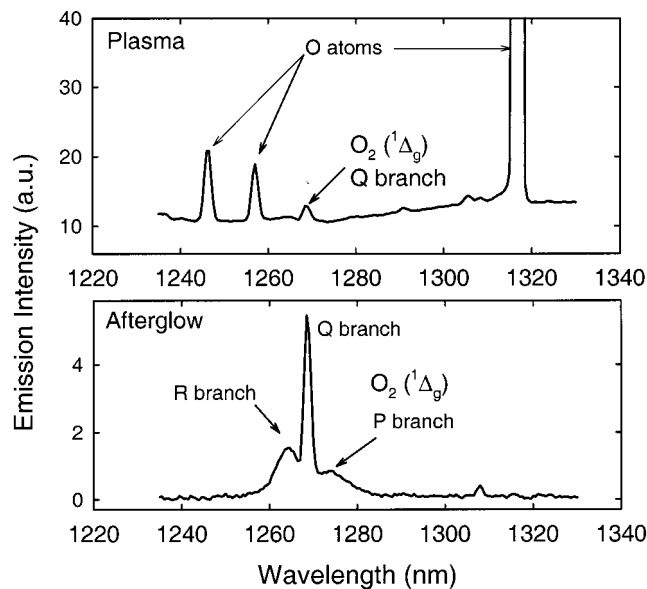*J. Phys. Chem. A, Vol. 104, No. 34, 2000* **8029**

Figure 3. Infrared emission spectrum of the plasma and the afterglow for operation at 24.4 W/cm^3, 6.0 Torr of O$_2$ and 120 °C.

The value used for the Einstein *A*-coefficient is 0.085 s^{-1}, and corresponds to a 0 to 0 vibrational transition.[16] Higher vibrational levels are not considered, because the neutral temperature of the plasma is about 373 K, whereas the equivalent energy of the first vibrational state is more than 2000 K.[16] The spectrometer calibration constant is obtained from eq 1, then used in eq 2 to determine the emission rate, R_Σ, from the integrated intensity of the bands. Finally, the concentration of $^1\Sigma_g^+$ O$_2$ is obtained from eq 3. Transient measurements of the singlet-sigma metastable emission were also obtained using the pulsed plasma as described above. The standard deviations in these experiments are within 50%.

Singlet-Delta Metastable Oxygen. Singlet-delta metastable oxygen, O$_2$ ($^1\Delta_g$), emits in the infrared between 1.2 and 1.3 μm.[16,17] To record this spectrum, a liquid nitrogen cooled InGaAs detector was employed with the monochromator using a 600 groove/mm grating blazed at 1.5 μm and a slit width of 400 μm. To increase the collection efficiency of the weak singlet-delta emission, the fiber-optic bundle was replaced with a lens assembly. Shown in Figure 3 is a spectrum recorded of the plasma while RF power was being applied to the electrodes. Peaks at 1246, 1257, and 1316 nm are observed due to emission from oxygen atoms. The Q branch of the metastable spectrum is barely visible above the continuum at 1269 nm.

To eliminate the background, a lock-in amplifier was utilized with an optical chopper, which was mounted in front of the lens as indicated in Figure 2b, and run at 50 and 100 Hz. The RF power supply was pulsed by the trigger signal with a duty factor of 45%. By adjusting the delay between the chopper and the RF power supply, only the light emitted during the afterglow was allowed to enter the spectrometer. The signal from the InGaAs detector was passed through a lock-in amplifier and on to an A/D converter and the computer for data acquisition. The signal varied as the monochromator swept through the wavelengths, thereby producing the singlet-delta spectrum shown in the lower half of Figure 3. Clearly visible are the P, Q, and R branches at 1264, 1269, and 1274 nm. The spectral resolution was 0.5 nm.

The singlet-delta emission, O$_2$ (a$^1\Delta_g$) to O$_2$ (X$^3\Sigma_g^-$) is very weak, a hundred times less intense than the singlet-sigma emission, O$_2$ (b$^1\Sigma_g^+$) to O$_2$ (X$^3\Sigma_g^-$). This makes calibration directly from the mercury/argon lamp difficult. An alternative

solution that we employed was to bridge the intensity range between the lamp and the singlet-delta signal using the moderately intense helium line at 1083 nm. Using eqs 1−3 above, but with the Einstein coefficient for the delta state, 2.58 × 10^{-4} s^{-1},[16] the concentration of O$_2$ (a$^1\Delta_g$) was obtained for one operating condition of 400 W RF power and 6 Torr of oxygen. This measurement provided a calibration factor (concentration/signal intensity) that could be used for other process conditions, where the signal was recorded as described below.

To determine the concentration of singlet-delta oxygen at other conditions, the signal intensity of the Q branch at 1269 nm was collected using the chopper arrangement depicted in Figure 2b. The detector signal decayed after the RF power pulse due to the reaction of O$_2$ (a$^1\Delta_g$) with O$_3$. The rate of this reaction is given by 6.01 × 10^{-11} exp($-2853/T$) × [O$_3$] × [O$_2$ $^1\Delta_g$].[18] Since the concentration of ozone is known as a function of the process conditions from the UV absorption measurements, a mass balance for O$_2$ (a$^1\Delta_g$) can be solved to yield a relationship between the initial concentration of O$_2$ (a$^1\Delta_g$) and the integral of the concentration dependence on time. The latter integral is proportional to the signal generated by the lock-in amplifier. Therefore, by using the known concentration of singlet-delta oxygen measured at 400 W and 6 Torr of O$_2$, the concentration at any other plasma condition can be obtained from the mass balance and the signal recorded from the lock-in amplifier. The uncertainty in this measurement is estimated to be within ±50% of the reported value.

III. Model

A numerical model has been developed to simulate the chemical kinetics that occurs after the RF power has been turned off for periods of time greater than 10 μs. After this short time has elapsed, one can neglect the influence of the charged species and the metastable states of helium and oxygen atoms on the reaction chemistry. In this case, the only species that need to be included in the kinetic model are ground-state O$_2$, O$_3$, He, and O atoms, and the two forms of metastable O$_2$, a$^1\Delta_g$ and b$^1\Sigma_g^+$. This assumption is justified on the basis of calculations of the lifetimes of the charged particles and the metastable atoms. The recombination coefficient for ions and electrons at atmospheric pressure is approximately 10^{-6} cm^3/s,[19] yielding a charged particle density of only 10^{11} cm^{-3} after 10 μs. This value is well below the concentrations of the reactive neutral species, which are in the range of 10^{15} cm^{-3} (see below).

With regard to metastable He (^{3}S$_1$) and O (^{1}D), these excited states are rapidly quenched by reaction with O$_2$. Both exhibit a pseudo first-order rate constant of about 10^7 s^{-1} at O$_2$ concentrations of 10^{17} cm^{-3}.[20,21] Consequently, their lifetimes are only 0.1 μs in our experiments. Similarly, metastable O (^{1}S) is quenched by reaction with O$_3$. Given a rate constant of 5.8 × 10^{-10} cm^3/s,[22] and an ozone concentration of 2 × 10^{15} cm^{-3}, the lifetime of this metastable state is less than 1 μs.

The transient material balance for each of the six species considered in the model is

$$\frac{d[X]}{dt} = \sum_i R_i \qquad (5)$$

where [X] is the concentration of species X, and R_i is the rate of reaction *i* that either produces or consumes X. The reactions employed and the corresponding kinetic constants are presented in Table 1. A thermal energy balance was not required, because the system may be assumed to be isothermal. A maximum adiabatic temperature rise of 0.1 °C was calculated. The set of

8030 *J. Phys. Chem. A, Vol. 104, No. 34, 2000*

Jeong et al.

TABLE 1: Reactions and Their Kinetic Constants

	reactions	rate constants (cm^3 molecule^{-1} s^{-1})	ref
R$_1$	$O + O + M \rightarrow O_2 + M$	$5.2 \times 10^{-35} \cdot \exp(900/T)$*,†	23
R$_2$	$O + O_2 + M \rightarrow O_3 + M$	$1.85 \times 10^{-35} \cdot \exp(1057/T)$*,‡	24
R$_3$	$O + O_3 \rightarrow O_2 + O_2$	$1.5 \times 10^{-11} \cdot \exp(-2250/T)$	23
R$_4$	$O_3 + M \rightarrow O + O_2 + M$	$7.26 \times 10^{-10} \cdot \exp(-11400/T)$‡	23
R$_5$	$O_2\,(^1\Delta_g) + He \rightarrow O_2 + He$	8.0×10^{-21}	25
R$_6$	$O_2\,(^1\Delta_g) + O_2 \rightarrow 2O_2$	$5.0 \times 10^{-18} \cdot \exp(-280/T)$	26
R$_7$	$O_2\,(^1\Delta_g) + O \rightarrow O_2 + O$	1.65×10^{-16}	26
R$_8$	$O_2\,(^1\Delta_g) + O_3 \rightarrow O + 2O_2$	$6.01 \times 10^{-11} \cdot \exp(-2853/T)$	18
R$_9$	$O_2\,(^1\Delta_g) \rightarrow O_2 + h\nu$	3.7×10^{-4}§	27
R$_{10}$	$2O_2\,(^1\Delta_g) \rightarrow O_2\,(^1\Sigma_g{}^+) + O_2$	$1.81 \times 10^{-19} \cdot (T/300)^{3.8} \cdot \exp(700/T)$	28
R$_{11}$	$O_2\,(^1\Sigma_g{}^+) + He \rightarrow O_2 + He$	1.0×10^{-17}	25
R$_{12}$	$O_2\,(^1\Sigma_g{}^+) + O_2 \rightarrow 2O_2$	1.0×10^{-16}	27
R$_{13}$	$O_2\,(^1\Sigma_g{}^+) + O \rightarrow O_2 + O$	8.0×10^{-14}	29
R$_{14}$	$O_2\,(^1\Sigma_g{}^+) + O_3 \rightarrow O + 2O_2$	1.5×10^{-11}	29
R$_{15}$	$O_2\,(^1\Sigma_g{}^+) \rightarrow O_2 + h\nu$	0.14 §	27

* Unit [=] cm^6/molecules^2/s. † Collision efficiencies, 0.62 for He and 1.15 for O$_2$. ‡ Collision efficiencies, 1.0 for oxygen and 0.54 for He, 0.13 for O, 2.27 for O$_3$. § Unit [=] 1/s.

Figure 5. The dependence of the O, O$_2$ ($^1\Delta_g$), O$_2$ ($^1\Sigma_g{}^+$), and O$_3$ concentrations on time and distance for initial plasma operation at 24.4 W/cm^3, 6.0 Torr of O$_2$, and 120 °C (symbols are the experimental data, whereas the lines are the model prediction).

As the gas emerges from the plasma at 55 mm, the concentration of ozone rapidly increases and approaches a new steady-state value at a distance of about 80 mm. The jump in ozone concentration in the afterglow rises with the oxygen partial pressure. At 15.2 Torr of O$_2$, the O$_3$ concentrations inside and outside the plasma are 0.4 and 1.0 × 10^{16} cm^{-3}, respectively. The change in ozone concentration is due to the reaction of O atoms with O$_2$ (R$_2$ in Table 1), and is an approximate measure of the O atom concentration in the plasma, ~6 × 10^{15} cm^{-3}.

Presented in Figure 5 is the evolution of the oxygen atoms, metastable oxygen molecules, and ozone with time after turning off the power to the electrode. The curves are the concentrations predicted from the numerical model, whereas the symbols are the experimental data. Excellent agreement is achieved between the theory and the experiment, without any adjustment to the rate constants. At time $t = 10\ \mu$s after the RF power is shut off, the concentrations of the five oxygen species are 1.3 × 10^{17} cm^{-3} ground-state O$_2$, 6.0 × 10^{15} cm^{-3} O atoms, 5.0 × 10^{15} cm^{-3} O$_2$ ($^1\Delta_g$), 1.0 × 10^{15} cm^{-3} O$_2$ ($^1\Sigma_g{}^+$), and 2.5 × 10^{15} cm^{-3} O$_3$. Assuming the concentrations of the neutral species are continuous from the on- to the off-state, these results indicate that the plasma converts 2% and 3.5% of the oxygen fed into O atoms and singlet-delta metastable O$_2$ molecules, respectively, at 6 Torr of O$_2$ and 24.4 W/cm^3 (400 W applied power).

After the discharge has been extinguished, the oxygen atoms rapidly recombine with oxygen molecules to produce ozone. The ozone concentration climbs to a constant value of 5 × 10^{15} cm^{-3} after about 3 ms, and does not change further. Note that the half-life of ozone decaying via reaction R$_4$ is 200 s at 120 °C. After 3 ms, the concentration of oxygen atoms has declined to about 1.0 × 10^{15} cm^{-3}. Thereafter, the amount of this species falls rapidly. The two metastable oxygen molecules, ($^1\Delta_g$) and ($^1\Sigma_g{}^+$), exhibit dramatically different decay rates. The singlet-delta state persists out to about 10 ms, whereas the singlet-sigma state is essentially extinguished by 500 μs. The consumption rate of both of these species is governed by their reaction with ozone, R$_8$ and R$_{14}$, respectively. The ratio of the rate constants for these two reactions at 120 °C is $k_8/k_{14} = 0.0038$.
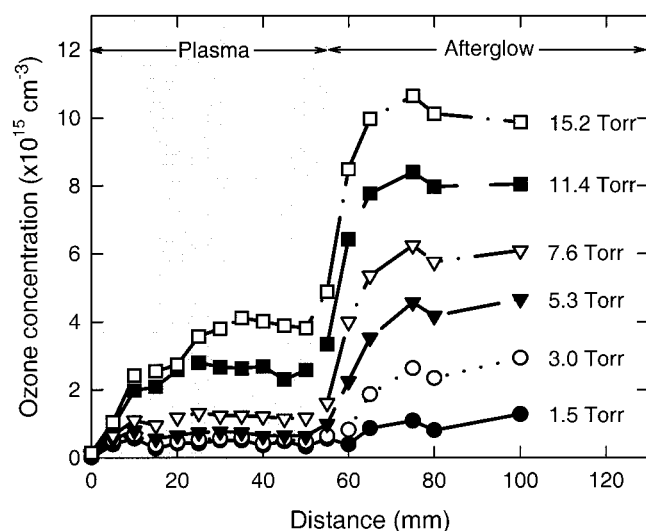

Figure 4. The dependence of the ozone concentration on axial position and oxygen partial pressure for an applied power of 24.4 W/cm^3 and a gas temperature of 120 °C.

five coupled, first-order differential equations were solved by the Runge−Kutta method using a Fortran program. The concentrations of all the species, except the ground-state oxygen atoms, were known at the initial condition, $t = 10\ \mu$s. The latter concentration was obtained by trial and error: different values were input to the model until a best fit was obtained to the measured concentration profiles for O$_2$ ($^1\Sigma_g{}^+$) and O$_3$. The rate constants obtained from the literature were used without modification.

IV. Results and Discussion

Concentration of the Reactive Species. Shown in Figure 4 are axial concentration profiles for ozone at different inlet pressures of oxygen. The plasma is observed over the RF electrode, which extends for 55.0 mm in the axial flow direction. For O$_2$ pressures below 10 Torr, the ozone concentration reaches a steady-state value 10 mm past the leading edge of the powered electrode. At 11.4 and 15.2 Torr of O$_2$, steady state is achieved at a distance of 30 mm. A similar behavior is observed for the singlet-sigma metastable oxygen emission. It should be noted that time-resolved measurements of the afterglow taken in the pulsed-plasma mode were acquired with the beam path directed across the duct at an axial distance of 45 mm.
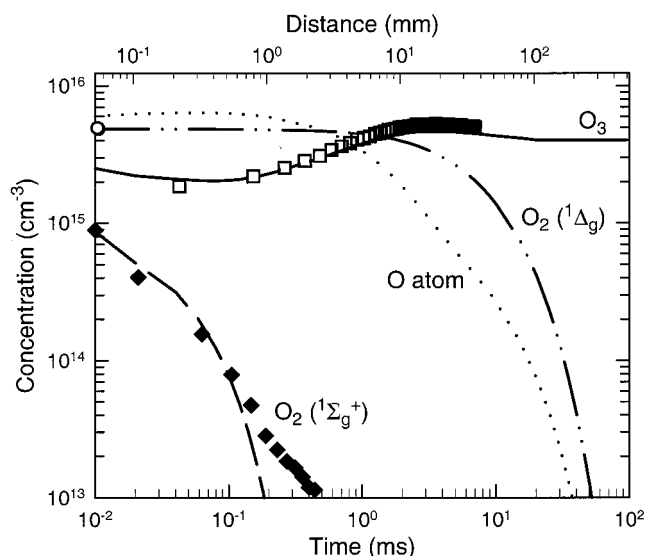
Reactions in Afterglow of Oxygen−Helium Plasma

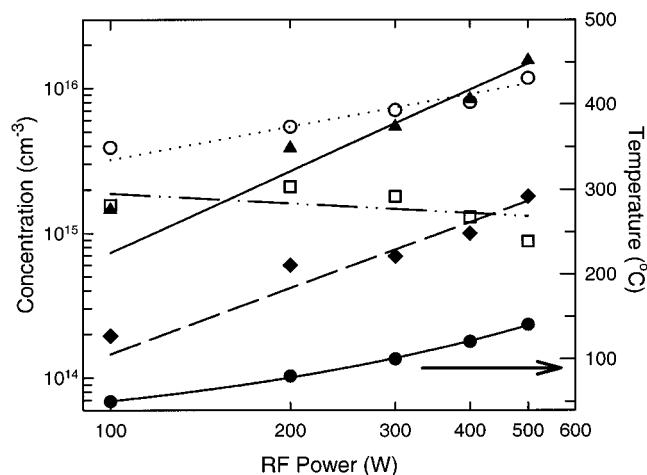*J. Phys. Chem. A, Vol. 104, No. 34, 2000* **8031**

Figure 6. The effect of the RF power on the concentrations of O atoms (▲), O_2 ($^1\Delta_g$) (○), O_2 ($^1\Sigma_g^+$) (◆), O_3 (□), and temperature (●) at 6.0 Torr O_2.

Figure 7. The effect of the oxygen pressure on the concentrations of O atoms (▲), O_2 ($^1\Delta_g$) (○), O_2 ($^1\Sigma_g^+$) (◆), and O_3 (□) at 24.4 W/cm^3 and 120 °C.

Figure 8. The evolution of the oxygen atom and ozone concentrations with time as predicted from the model with (open symbols) and without (filled symbols) metastable oxygen molecules included. The initial plasma conditions are 24.4 W/cm^3, 6.0 Torr of O_2, and 120 °C.

In Figure 5, distance is plotted on the upper *x* axis so that one can also examine how the reaction evolves as the gas travels downstream in the afterglow region. The linear velocity of the gas between the electrodes is 5.2 m/s, so that 1 mm equals 192 μs. It is interesting to note that the spatial resolution of the measurements was 3 mm. By contrast, the resolution obtained with the transient measurements was 2 μs, a 300-fold improvement. Inspection of the figure reveals that the concentration of oxygen atoms remains constant out to 1 mm, then drops by a factor of 3 on going from 1 to 10 mm. Since the O atoms are the most reactive species, and would be desired in many materials-processing applications, these results suggest that the substrate should be placed within 1 to 2 mm of the exit of the plasma.

Shown in Figure 6 is the effect of the RF power on the concentrations of O atoms, O_2 ($^1\Delta_g$), O_2 ($^1\Sigma_g^+$), and O_3, which are present 10 μs after the RF power has been turned off. Note that the neutral temperature in the plasma rises from 60 °C at 100 W to 140 °C at 500 W. The log−log plot shows that all the species increase with the RF power except for ozone. The slopes of the "best-fit" lines yield the following dependencies: $O \propto P_{RF}^{1.9}$, O_2 ($^1\Delta_g$) $\propto P_{RF}^{0.8}$, O_2 ($^1\Sigma_g^+$) $\propto P_{RF}^{1.5}$, and $O_3 \propto P_{RF}^{-0.2}$.

Presented in Figure 7 is the effect of the oxygen partial pressure on the concentrations of O atoms, O_2 ($^1\Delta_g$), O_2 ($^1\Sigma_g^+$), and O_3, which are present 10 μs after the RF power has been turned off. Except for singlet-sigma metastable oxygen, the concentrations of the reactive species increase with the oxygen pressure throughout the range studied. The strongest dependence is seen for ozone, as expected because it requires two oxygen molecules to be produced. The dependencies on oxygen pressure obtained from the best-fit lines to the data are $O \propto P_{O_2}^{0.6}$, O_2 ($^1\Delta_g$) $\propto P_{O_2}^{0.5}$, O_2 ($^1\Sigma_g^+$) $\propto P_{O_2}^{-0.2}$, and $O_3 \propto P_{O_2}^{1.5}$.

Shibata et al.[30] have modeled the structure of an oxygen discharge in a parallel-plate reactor driven with 150 W RF power at 13.56 MHz and a total oxygen pressure of 0.5 Torr. They predict an average number density for oxygen atoms of ∼3 × 10^{14} cm^{-3}. Extrapolating the data in Figures 6 and 7 to 0.5 Torr of O_2 and 150 W, yields a value of ∼5 × 10^{14} cm^{-3} for our glow discharge source. This value is in good agreement with Shibata's work.

Analysis of the Reaction Kinetics. A series of simulations have been run to determine which reactions listed in Table 1 are kinetically significant. We have found that only seven are needed to describe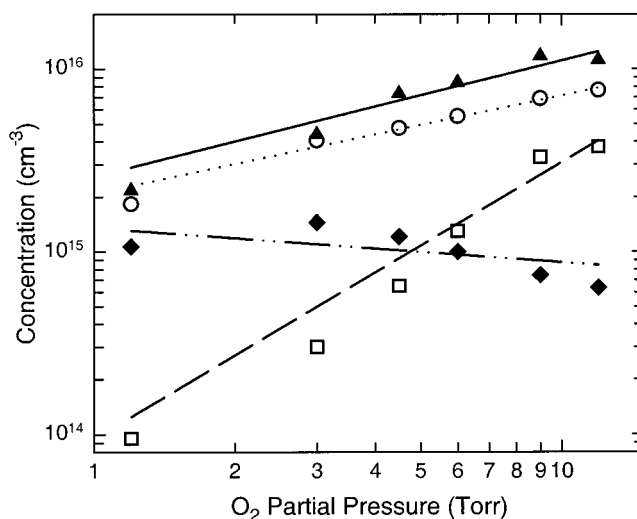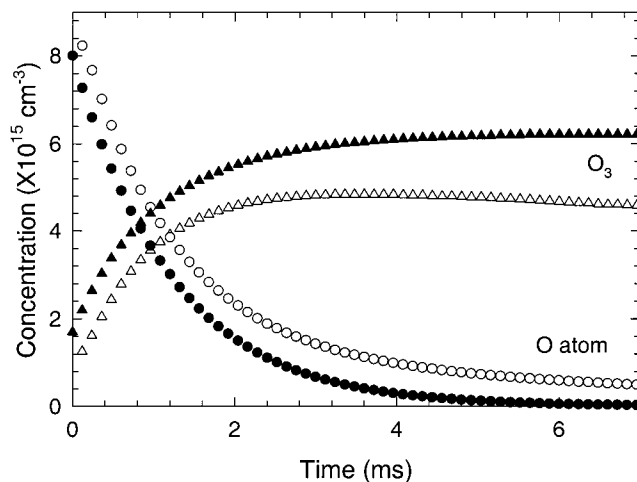 the chemistry in the afterglow, R_1, R_2, R_3, R_8, R_{11}, R_{13}, and R_{14}. The first three of these, R_1, R_2, and R_3, consume oxygen atoms, and account for most of the ozone production. The fourth, R_8, converts singlet-delta metastable oxygen molecules and ozone into ground-state oxygen atoms and molecules. The last three reactions, R_{11}, R_{13}, and R_{14}, extinguish the singlet-sigma metastable oxygen molecules by collision with other species in the gas. As shown in Figure 5, the collisional de-excitation of O_2 ($^1\Sigma_g^+$) occurs rapidly within the first hundred microseconds. Since this molecule decays so fast and has a negligible influence on the other reactive species, the mechanism may be simplified further to include just reactions R_1, R_2, R_3, and R_8.

In an earlier study of the atmospheric-pressure plasma, we proposed that the afterglow could be modeled with only three reactions involving the consumption of O atoms and the production of ozone (R_1, R_2, and R_3).[10] In the present work, we have found that this mechanism must be modified to add in the effects of singlet-delta metastable oxygen. The plasma generates this molecule in about the same abundance as the oxygen atoms. The impact of O_2 ($^1\Delta_g$) on the concentrations of O atoms and O_3 in the afterglow is illustrated in Figure 8. The long-lived metastable molecules become a source of oxygen atoms via reaction R_8, so that the O atoms persist for a much

greater period of time (>10 ms), albeit at concentrations near 1×10^{14} cm^{-3}. In addition, if the O$_2$ ($^1\Delta_g$) is omitted from the model, it over-predicts the generation of ozone by about 50%.

When all the reactions taking place in the effluent are compared, those that either produce or consume ozone dominate in the afterglow ($t > 10$ μs). For example, reaction R$_2$ is about 1 order of magnitude faster than the other significant reactions of O atoms, R$_1$ and R$_3$. With regard to the metastable molecules, O$_2$ ($^1\Sigma_g^+$) and O$_2$ ($^1\Delta_g$), they are quenched by ozone at rates that are several hundred times faster than their reactions with other species.

On the basis of experimentally determined concentration profiles for O$_2$ ($^1\Sigma_g^+$) and O$_3$, the rate constant for O$_2$ ($^1\Sigma_g^+$) quenching reaction, R$_{14}$, can be evaluated. When only this step is considered, the mass balance for O$_2$ ($^1\Sigma_g^+$) is

$$\frac{d[O_2\ ^1\Sigma_g^+]}{dt} = -k_{14}[O_2\ ^1\Sigma_g^+][O_3] \tag{7}$$

This form of the rate constant only holds under the assumption that the other reactions involving O$_2$ ($^1\Sigma_g^+$) are much smaller than its quenching rate with O$_3$. In the afterglow, this is true for about 80 μs. At longer times, the energy pooling reaction, R$_{10}$, is comparable in magnitude to R$_{14}$. At 400 W and O$_2$ pressures varying from 1 to 12 Torr, an average value of k_{14} has been calculated. In this case, the rate constant equals (1.1 ± 0.3) $\times 10^{-11}$ cm^3/s. This number is in good agreement with the value of 1.5×10^{-11} cm^3/s reported by Watson and co-workers.[29]

Etching Polyimide Films. We have etched polyimide films with the parallel-plate device used in the present study. In this case, the film was placed on the aluminum oxide plate located just downstream of the plasma (Figure 1). The etching rate of the polyimide at 225 °C equals 4.2 μm/min at the leading edge adjacent to the plasma, but declines rapidly with distance to essentially 0.0 μm/min at 20 mm downstream. Perusal of Figure 5 reveals that the oxygen atoms are the only reactive species with a decay profile that is similar to the fall-off in the etching rate of the polyimide. These results substantiate our earlier conclusion that oxygen atoms are the principal active species in the etching of organic films with the atmospheric-pressure plasma.[10]

V. Conclusions

The concentration of ground-state O atoms, metastable oxygen molecules, a$^1\Delta_g$ and b$^1\Sigma_g^+$, and ozone in the downstream region of an atmospheric-pressure oxygen and helium discharge has been determined by a combination of optical spectroscopy and numerical modeling of the reaction kinetics. The dependence of the concentrations of the reactive intermediate, O (^{3}P), O$_2$ (a$^1\Delta_g$), O$_2$ (b$^1\Sigma_g^+$), and O$_3$, on the RF power and oxygen partial pressure has been determined. Oxygen atoms are found to be the principal active species responsible for etching organic thin films.

References and Notes

(1) Hartney, M. A.; Hess, D. W.; Soane, D. S. *J. Vac. Sci. Technol. B* **1989**, *7*, 1.

(2) Lieberman, M. A.; Lichtenberg, A. J. *Principles of Plasma Discharges and Materials Processing*; John Wiley & Sons: New York, 1994; p 324.

(3) Grill, A. *Cold Plasma in Materials Fabrication from Fundamentals to Applications*; IEEE Press: New York, 1994.

(4) Brake, M.; Hinkle, J.; Asmussen, J.; Hawley, M.; Kerber, R. *Plasma Chemistry and Plasma Processing* **1983**, *3*, 63.

(5) Noxon, J. F. *Can. J. Phys.* **1961**, *39*, 1110.

(6) Borrel, P.; Richards, D. S. *J. Chem. Soc., Faraday Trans. 2* **1989**, *85*, 1401.

(7) Kruger, D. H.; Owano, T. G.; Laux, C. O. *IEEE Trans. Plasma Sci.* **1997**, *25*, 1042.

(8) Braun, A. E. *Semicond. Int.* **1999**, *22*, 64.

(9) Jeong, J. Y.; Babayan, S. E.; Tu, V. J.; Park, J.; Henins, I.; Velarde, J.; Hicks, R. F.; Selwyn, G. S. *Plasma Sources Sci. Technol.* **1998**, *7*, 282.

(10) Jeong, J. Y.; Babayan, S. E.; Schuetze, A.; Tu, V. J.; Park, J.; Henins, I.; Selwyn, G. S.; Hicks, R. F. *J. Vac. Sci. Technol. A* **1999**, *17*, 2581.

(11) Babayan, S. E.; Jeong, J. Y.; Tu, V. J.; Park, J.; Hicks, R. F.; Selwyn, G. S. *Plasma Sources Sci. Technol.* **1998**, *7*, 286.

(12) Schütze, A.; Jeong, J. Y.; Babayan, S. E.; Park, J.; Selwyn, G. S.; Hicks, R. F. *IEEE Trans. Plasma Sci.* **1998**, *26*, 1685.

(13) Inn, E. C. Y.; Tanaka, Y. J. *J. Opt. Soc. Am.* **1953**, *43*, 870.

(14) Vigroux, E. *Ann. Phys.* **1953**, *8*, 709.

(15) Ny, T. Z.; Choong, S. P. *Chin. J. Phys.* **1933**, *1*, 38.

(16) Krupenie, P. H. *J. Phys. Chem. Ref. Data* **1972**, *1*, 423.

(17) Pearse, R. W. B.; Gaydon, A. G. *The Identification of Molecular Spectra*; Wiley: New York, 1976.

(18) Gallagher, J.; Beaty, E.; Dutton, J.; Pitchford, L. *J. Phys. Chem. Ref. Data* **1983**, *12*, 109.

(19) Biondi, M. A. *Principles of Laser Plasmas*; Bekefi, G., Ed.; Wiley: New York, 1976; Chapter 4.

(20) Bortner, M. H.; Bauer, T. *Defense Nuclear Agency Reaction Rate Handbook*, 2nd ed.; DASIAC: Santa Barbara, CA, 1972.

(21) Davidson, J. A.; Sadowski, C. M.; Schiff, H. I. *J. Chem. Phys.* **1976**, *64*, 57.

(22) Smirnov, B. M. *Excited atoms*; Energotomizdat: Moscow, 1982.

(23) Hampson, R. F.; Garvin, D. *Reaction Rate and Photochemical Data for Atmospheric Chemistry-1977, NBS Special Publication 513*; U.S. Government Printing Office: Washington, DC, 1978.

(24) Sabadil, H.; Bachmann, P.; Kastelewicz, H. *Beitr. Plasmaphys.* **1980**, *20*, 283.

(25) Frimer, A. *Singlet O₂, Vol. I, Physical-Chemical Aspects*; CRC Press: Boca Raton, FL, 1985.

(26) Eliasson, B.; Kogelschatz, U. *Basic Data for Modeling of Electrical Discharges in Gases: Oxygen*; Asea Brown Boveri: Baden, Switzerland, 1986.

(27) Heicklen, J. *Atmospheric Chemistry*; Academic Press: New York, 1976.

(28) Cohen, N.; Westerberg, K. *J. Phys. Chem. Ref. Data* **1983**, *12*, 531.

(29) Baulch, D.; Cox, R.; Crutzen, P.; Hampson, R.; Kerr, J.; Troe, J.; Watson, R. *J. Phys. Chem. Ref. Data* **1982**, *11*, 327.

(30) Shibata, M.; Nakano, N.; Makabe, T. *J. Appl. Phys.* **1995**, *77*, 6181.